

CONTROLS ON THE FREQUENCY CONTENT OF NEAR-SOURCE INFRASOUND
AT AN OPEN-VENT VOLCANO (VILLARRICA, CHILE)

by

Bryan Blake Rosenblatt



A thesis

submitted in partial fulfillment

of the requirements for the degree of

Master of Science in Geophysics

Boise State University

December 2021

© 2021

Bryan Blake Rosenblatt

ALL RIGHTS RESERVED

BOISE STATE UNIVERSITY GRADUATE COLLEGE

DEFENSE COMMITTEE AND FINAL READING APPROVALS

of the thesis submitted by

Bryan Blake Rosenblatt

Thesis Title: Controls on the Frequency Content of Near-Source Infrasonics at an Open-Vent Volcano (Villarrica, Chile)

Date of Final Oral Examination: 27 October 2021

The following individuals read and discussed the thesis submitted by student Bryan Blake Rosenblatt, and they evaluated the student's presentation and response to questions during the final oral examination. They found that the student passed the final oral examination.

Jeffrey B. Johnson, Ph.D. Chair, Supervisory Committee

Jacob Anderson, Ph.D. Member, Supervisory Committee

Brian Jackson, Ph.D. Member, Supervisory Committee

The final reading approval of the thesis was granted by Jeffrey B. Johnson, Ph.D., Chair of the Supervisory Committee. The thesis was approved by the Graduate College.

ACKNOWLEDGMENTS

First and foremost, must acknowledge my advisor, Dr. Jeffrey Johnson, for recruiting me onto his research team as a young physicist with no background in geoscience. Jeff has been there for me at all turns of my master's track and his help and wisdom have been invaluable to me as a person and scientist.

Thank you to my committee members, Jake Anderson and Brian Jackson, for bouncing ideas back and forth with me, proofreading my work, and holding me to a high standard. Brian Jackson gave me a baseline knowledge for classical mechanics during my undergraduate physics degree and has helped me throughout my scientific process as a master student, affording me a perspective different than those in the geosciences. Jake Anderson has helped me with an uncountable amount of problems involving coding, electronics, and my own ideas. I am grateful to be under the guidance of both of these inspirational scientists.

I would also like to thank everyone who travelled to Chile with me to help collect the data used for this research. This field work was pivotal for my academic career and this paper would not be here without these individuals: Jeff Johnson, Jake Anderson, Scott Gauvain, Jerry Mock, Ashley Bosa, Kristina Rossavik, Kate Bollen, Rainey Aberle, Leighton Watson, Oliver Lamb, John Browning, Julian Traphagan, Madeline Hunt, and each of the Chilean guides who helped us climb Villarrica.

Of course, I need to give a huge thanks to all of my family, but most specifically my parents. They are always by my side pushing me to be the best that I can be. Thanks Mom and Dad.

My girlfriend, Amanda Kuhlman, held me up during my best, and more importantly, during my worst. I can honestly say I wouldn't be here with this document without her.

Lastly, I would like to thank all of the individuals who didn't fall into any of these groups. Alex Witsil, Armando Pineda, Landon Lemieux, Keehoon Kim, and more. While this work is my own, it comes from years of guidance, problem solving, learning, chatting, and everything else that my communities have afforded me.

This work was partially supported by a National Science Foundation Grant EAR-1830976.

ABSTRACT

The acoustic signals from open-vent volcanoes can contain specific information related to that volcano's eruption dynamics and future activity. Thus, studying a specific volcano's acoustics may provide critical warning mechanisms, signaling impending eruptions. Villarrica volcano, located in southern Chile, has an active lava lake that produces continuous infrasound with spectral peaks near 1 Hz and excursions of $\pm \sim 0.2$ Hz. The infrasound's frequency content reveals key volcanic properties such as eruption style and crater shape. Leading up to Villarrica's most recent paroxysm in 2015, infrasound spectral changes coincided with and indicated a rise in Villarrica's lava lake level. As such, quantifying and understanding the regular fluctuation in recorded infrasonic frequencies, from Villarrica and other open-vent volcanoes, is imperative. A week-long period of crater rim infrasound observations associated with stable, open-vent activity, revealed two independent source processes: spatter bursting events and lava lake-induced tremor oscillations (broadband discrete signals and ~ 1 Hz tremor respectively). Comparison of these acoustic signals with results from a 3-D finite-difference time-domain wave propagation model (InfraFDTD) shows that sound speed and source spectrum variability can both influence Villarrica's spectrum. Yet, sound speed variations in the crater--whether diurnal or volcanic in origin--cannot explain the full extent of the observed frequency excursions. Instead, source spectrum variability is primarily responsible for the frequency excursions. This work highlights the utility of

data collected from a dense distribution of twenty infrasound sensors operating at the summit and validates the effectiveness of the InfraFDTD modeling approach.

TABLE OF CONTENTS

ACKNOWLEDGMENTS	iv
ABSTRACT	vi
LIST OF FIGURES	x
LIST OF ABBREVIATIONS.....	xii
CHAPTER ONE: INTRODUCTION.....	1
1.1 Volcano Acoustics	2
1.2 Villarrica Volcano	3
1.3 The Scope of the Study	4
CHAPTER TWO: DATA AND METHODS.....	6
2.1 Data and Data Collection	6
2.2 InfraFDTD Wave Propagation Model	8
CHAPTER THREE: RESULTS AND DISCUSSION.....	15
3.1 Spatial and Temporal Frequency Fluctuations	15
3.2 InfraFDTD Outputs.....	20
3.2.1 Sound Speed.....	21
3.3 Villarrica’s Infrasound Sources	23
3.3.1 The Continuous Infrasound source	23
3.3.2 The Impulsive Infrasound Source	23
3.4 Synthetic Infrasound Source-Time Function	27

CHAPTER FOUR: IMPLICATIONS AND CONCLUSION	30
4.1 The Implications	30
4.1.1 Importance.....	30
4.1.2 Limitations	31
4.1.3 Future Work	32
4.2 Conclusion	32
REFERENCES.....	34

LIST OF FIGURES

Figure 2.1	Digital elevation model (DEM) of Villarrica’s summit showing locations of 20 sensors.	7
Figure 2.2	Example time-series infrasound showing signal recorded at six (of the twenty) stations recording at the summit of Villarrica on 17 January 2020. (a) The 720 s waveform contains continuous ~1 Hz infrasound as well as four discrete events occurring at -310s, -250s, 110s, and 160s. Panels (a) and (b) have normalized amplitudes whereas panel (c) shows amplitudes in Pa.....	8
Figure 2.3	Examples of two model runs with 350 m/s sound speed and a Blackman-Harris volumetric flow source function (a) at 1.5 Hz and (d) at 2.5 Hz. (b, e) Normalized synthetic signals at the sensor positions shown as receiver gathers. (c, f) Spectra of synthetic signals for all stations along with source input frequency spectrum (black curve).....	12
Figure 2.4	(a)-(f) Day-long histograms of peak frequencies for six different stations and best-fit normal distribution (red trace) showing 25th and 75th percentiles (yellow bars). Peak frequencies are calculated with 100 second windows and 50% overlap, resulting in ~1,700 windows grouped into 50 bins.	14
Figure 3.1	(a)-(f) Day-long spectrograms from January 18, 2020, for the 6 stations indicated in Figure 2.4. The peak amplitude frequency has been indicated with a red line. Window duration is 100 s with 50% overlap. Spectral content has been filtered above a 0.55 Hz corner.	17
Figure 3.2	X-Y scatter plot comparing the peak frequencies recorded from station s010 (I) and s100 (O). The dashed black line indicates where the perfect correlation between sensors is.	18
Figure 3.3	(a) Box-and-whisker spatial peak frequency plot. Each box contains twenty peak frequency values (one per station) for a 100 s window. The window is then advanced by 50 s (50%) and recalculated. Box limits correspond to 25 and 75 percentiles and whiskers encapsulate 95% of data. (b) Time-series record (band-pass filtered between .55 and 5 Hz) from s010 (I) and s100 (O) showing the variations in infrasound tremor amplitude.	19

Figure 3.4	Box-and-whisker peak frequency plot for s010 (O) during the four coldest hours of the night (0:00-4:00, local time, black) and the four hottest hours of the day (11:00-15:00, local time, gray) for the week-long dataset. Box limits correspond to 25 and 75 percentiles and whiskers encapsulate 95% of data. Peak frequencies are calculated from spectrograms as in Figure 2.4 using 100 s windows and 50% overlap.20
Figure 3.5	Relationship between input Blackman-Harris source frequency (x-axis) and modeled peak frequency (y-axis) for a range of crater sound speeds. All model runs used a Blackman-Harris source function as an input. Dashed horizontal lines correspond to the range of peak frequencies recorded.21
Figure 3.6	Station s108 infrasound time-series and spectrogram associated with three small spattering/Strombolian events. a) 5 Hz high-pass filtered time-series showing significant energy above 5 Hz. b) 0.5 Hz high-pass filtered time series showing prevalent background tremor and high frequency components largely obscured. c) Spectrogram of the 0.5 Hz high-passed data calculated for 10 s intervals and 50% overlap.25
Figure 3.7	Impulse source-time function and modeled time series and spectra with 350 m/s sound speed. (a) Modeled Dirac delta pressure function band-pass filtered with 4 poles between 0.55 and 5 Hz. (b) Synthetic output for the distributions of sensors deployed at Villarrica. (c) Output amplitude spectra. The black curve indicates the source-time function spectrum.26
Figure 3.8	Images of Villarrica’s crater and schematic interpretation of geometry and sound wavelengths. a) UAV-based photograph of the inside of Villarrica’s crater taken on 15 January 2020 and showing a lava lake skylight as described by Palma et al. (2008) and Goto & Johnson (2011). b) Schematic cross section of the crater highlighting the continuous infrasound excited by movement of/from the lava lake. c) Image from crater rim showing a small Strombolian eruption on 16 January 2020. d) Schematic cross section of the crater during Strombolian activity showing 5 Hz infrasound wavelengths drawn approximately to scale.27
Figure 3.9	Deconvolution of crater acoustic response from tremor examples at 6 stations. (a) Band-passed impulse from Figure 3.7a. (b) Impulse response calculated for several stations from Figure 3.7b. (c) Tremor examples recorded at several stations from 18 January. (d, e, f) Spectra from panels a, b, c respectively. (g) Green’s functions for each station. (h) Deconvolved source inputs for each station from spectral division of recorded infrasound divided by Green’s functions.28

LIST OF ABBREVIATIONS

(C)	Crater
(I)	Inside
(O)	Outside
DEM	Digital Elevation Model
FDTD	Finite-Difference Time-Domain
GPU	Graphic Processing Units
OVDAS	Observatorio Volcanológico de los Andes del Sur
SfM	Structure from Motion

CHAPTER ONE: INTRODUCTION

Volcanic eruptions occur on an hourly basis across the globe with an incredibly wide range of magnitudes (none to global hazards), styles (Hawaiian effusive, Strombolian, Plinian, etc.), and precursors (none, earthquakes, tilt, tremor, etc.). In addition, these traits will vary temporally for a single volcanic system. The scientific understanding of each of these systems separately and as a whole is the study of volcanology. Like looking at a single cell in a petri dish through a microscope, analyzing the processes occurring at a single volcano can help elucidate the reasons behind specific volcanic behaviors. This type of analysis leads to one of the primary goals of volcanology, eruption forecasting and hazard mitigation. This thesis utilizes this core idea by closely analyzing the acoustic signal of Villarrica volcano, a volcano in southern Chile, during a time of relative stability.

Chapter 1 introduces volcano acoustics as well as the volcano in question, Villarrica, and the scope of the study. Chapter 2 details the data and data collection process, the finite-difference time-domain (FDTD) wave propagation model used, and distribution statistics for the spectral content of the infrasound data. Chapter 3 discusses results in the form of temporal and spatial frequency statistics and modelled parameter space limitations. This chapter also presents a speculative source-time function for Villarrica's low frequency acoustic waves. Lastly, Chapter 4 ends the paper with a discussion of implications and concluding remarks.

1.1 Volcano Acoustics

The behavior of most open-vent volcano can be appropriately characterized by its infrasound (low-frequency sounds below the 20 Hz threshold of human hearing) (Allstadt et al., 2018; Dzierma & Wehrmann, 2010; Goto & Johnson, 2011; Ripepe et al., 2010). One of, if not the, primary influences on an acoustic signal is geometry. Thus, the geometry of volcanic craters has previously been described as that of a massive horn (Johnson et al., 2018b; Richardson et al., 2014; Watson et al., 2019) or Helmholtz resonator (Fee et al., 2010; Goto & Johnson, 2011; Spina et al., 2014) capable of resonating in infrasonic frequencies. These sub-audible pressure waves contain key information related to the dynamics of volcanic processes (Marchetti et al., 2009; Spina et al., 2014; Vergnolle & Brandeis, 1994). Wave propagation models may elucidate these processes through calculation of Green's functions, which may be computed over a range of controllable properties (Watson et al., 2019). These models include the influence of crater geometry, temperature, and source functions (Kim & Lees, 2011; Kim et al., 2012; Lacanna & Ripepe, 2013; Taddeucci et al., 2012).

Examples of volcanic infrasound usage span a wide range. Cotopaxi Volcano's infrasound has revealed a relatively unchanged crater and conduit morphology throughout infrasound monitoring periods (Johnson et al., 2018a; Johnson & Watson, 2019). Resonant infrasound from the craters of Mt. Etna Volcano (Spina et al., 2014), or the deep conduit of Kilauea (Fee et al., 2010) has been used to calculate the lengths of their respective conduits. Remote volcanoes, such as most of the Alaskan infrasound producing volcanoes, (Mt. Cleveland, Bogoslof, Pavlof, etc.) can be monitored from 5-6 kilometers away due to the low attenuation rate and large propagation range of

infrasound signals (De Angelis et al., 2012; Schwaiger et al., 2020; Fee et al., 2017). The unique infrasound signal from the sub-marine volcano of Bogoslof led to the discovery of a large (>100-meter radius) underwater volcanic bubble acting as the primary infrasound source (Lyons et al., 2019). These examples highlight a few of the wide usages and advantages of volcanic infrasound monitoring.

1.2 Villarrica Volcano

Volcán Villarrica is an open-vent stratovolcano with an elevation of ~2800 m above sea level and a persistently active degassing lava lake within its crater (Palma et al., 2008). It is a part of the volcanic arc known as the Southern Volcanic Zone in southern Chile which is a result of the Nazca Plate subducting beneath the South American Plate. Villarrica formed in the Mid-to-Late Pleistocene era (~100 ka before present) and has remained active with a pattern of explosive collapses followed by rebuilding (Dzierma & Wehrmann, 2010). The explosive basaltic activity of Villarrica is characterized as a Strombolian eruption style with a variety of magnitudes (Gurioli et al., 2008).

Presently, Villarrica is one of the most active volcanoes in South America and one of Chile's most popular tourist destination. Since it sits in an area with high population density, even small eruptions pose hazards to the surrounding towns of Pucón and Villarrica (Dzierma & Wehrmann, 2010). More specifically, its glaciated summit poses a threat from approximately decadal paroxysmal eruptions and possible lahar generation (Johnson & Palma, 2015; Naranjo & Moreno, 2004; Van Daele et al., 2014)

Volcán Villarrica is a reliable laboratory for volcano infrasound studies due to its continuous production of infrasound (Goto & Johnson, 2011; Richardson & Waite, 2013;

Ripepe et al., 2010). In addition, its glaciated summit can produce icequakes which can interfere with the seismic signals (Lamb et al., 2020; Mora-Stock et al., 2014). With Villarrica being one of the most continually active volcanoes in Chile, multidisciplinary monitoring, including infrasound surveillance, is critical for proper hazard assessment in this populated and touristic region (Dzierma & Wehrmann, 2010). Villarrica's most recent eruption on 3 March 2015 was a short-lived but violent VEI 2 event (Romero et al., 2018). Just before this 2015 eruption, Johnson et al. (2018b) observed and modeled a rise in Villarrica's infrasonic frequency correlated to a rise in lava lake level.

1.3 The Scope of the Study

The field experiment in January of 2020 was designed to record Villarrica's infrasonic frequencies close to the source using a dense network of 20 sensors. Over the week-long recording period, volcanic activity was stable and there were no changes to the crater's geometry, no noticeable change of eruption styles, and no large explosive eruptions (i.e., ejecta leaving the crater rim). Although small spatter events from the lava lake were noted, the source and mechanism of Villarrica's continuous monotonic infrasound was largely unchanged compared to experiments with longer recording intervals (Johnson et al., 2018b; Richardson et al., 2014; Shinohara & Witter, 2005). Since the frequency content of Villarrica's infrasound has been proposed as a powerful forecasting tool (Johnson et al., 2018b), any slight frequency fluctuations, which must be unrelated to crater geometric changes, may reveal key information regarding the volcano's activity. This study focuses on non-geometric factors, such as the sound speed (i.e., temperature), infrasound source characteristics, and the spatial distribution of

sensors around the crater for understanding their impact on the observed frequency content during a stable monitoring period.

CHAPTER TWO: DATA AND METHODS

2.1 Data and Data Collection

Twenty Gem Infrasond Loggers (Anderson et al., 2018) recorded infrasond with a sample rate of 100 Hz, passband of 0.04-27 Hz (several octaves above and below the signals of interest), approximately 3 mPa resolution (quieter than both environmental noise and volcanic signals), and GPS time synchronization every second including date, time, and location. Seventeen sensors were situated around the crater, seven inside (I) and ten outside (O) the crater rim; the other three were situated on a cable (C) strung across the crater in an east/west orientation (Figure 2.1). These sensor's data is broadly classified based upon their position, O, I, or C.

Seventeen of the summit sensors recorded continuously for a full week starting on January 12, 2020, while three of the cable sensors were deployed later and recorded continuously for the last three days until January 19. Before analysis, all signals were band-pass filtered between 0.55 and 5 Hz using a fourth-order Butterworth filter. This was done in an effort to reduce microbarom noise below 0.5 Hz and wind noise at or above 5 Hz while still capturing the frequency band of interest associated with Villarrica (around 1 Hz). For conciseness, six geographically dispersed stations {c097 (C), s012 (I), s010 (I), s084 (I), s100 (O), and s094 (O)} are highlighted in figures and analyses. Example data, including background tremor and a few discrete bursts, is shown in Figure 2.2.

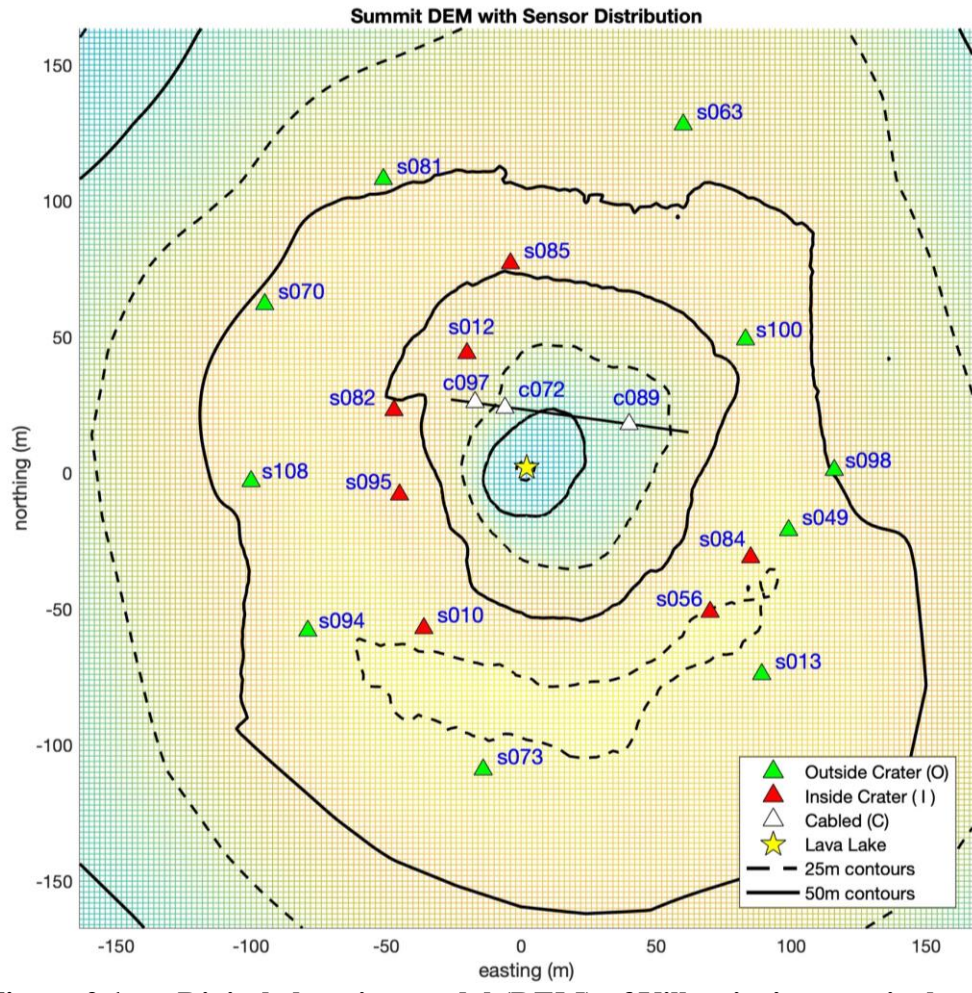


Figure 2.1 Digital elevation model (DEM) of Villarrica’s summit showing locations of 20 sensors.

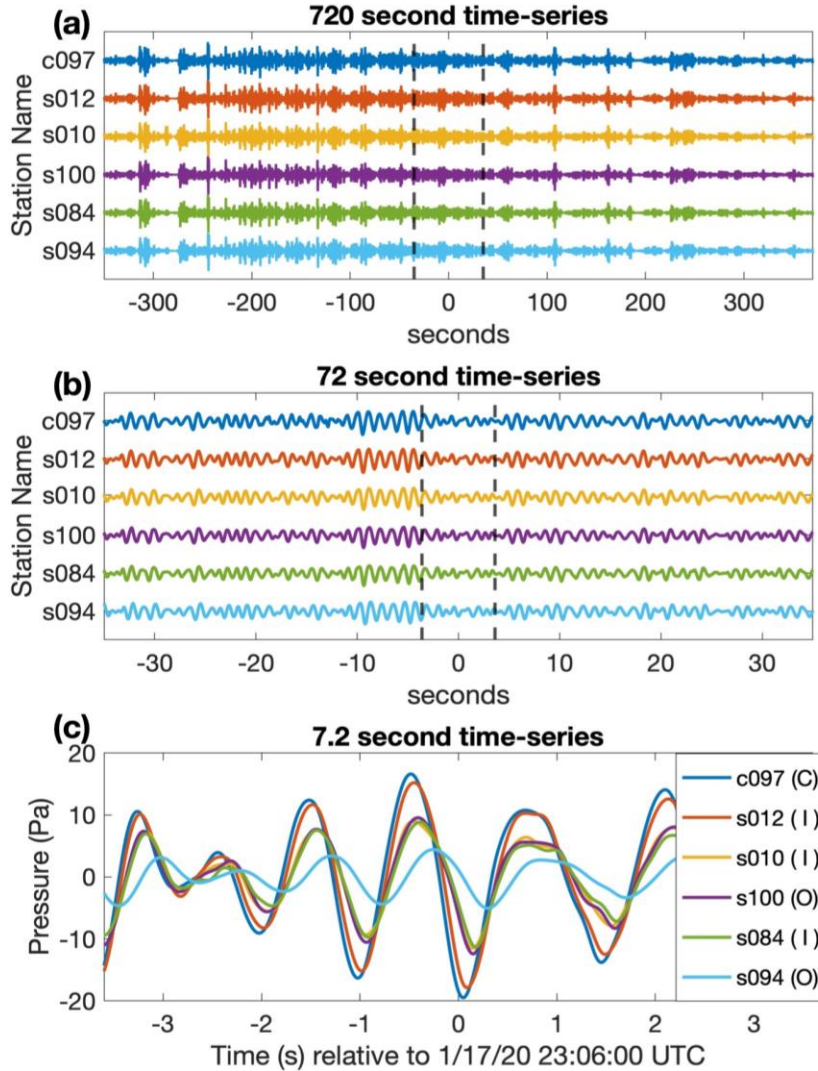


Figure 2.2 Example time-series infrasound showing signal recorded at six (of the twenty) stations recording at the summit of Villarrica on 17 January 2020. (a) The 720 s waveform contains continuous ~ 1 Hz infrasound as well as four discrete events occurring at -310s, -250s, 110s, and 160s. Panels (a) and (b) have normalized amplitudes whereas panel (c) shows amplitudes in Pa.

2.2 InfraFDTD Wave Propagation Model

To help interpret the differences among stations as well as what might be influencing these differences, a numerical modelling approach is taken. This numerical approach consists of a 3D FDTD acoustic wave propagation model used to quantify the influence of crater topography and atmospheric properties on the source-time functions. The digital elevation model (DEM) for the crater is a primary input for the model and it is

derived from drone-based structure-from-motion (SfM). I assume that both the DEM and the location of the lava lake at the bottom of the crater do not change over the week-long data acquisition interval, thus the system is linear. The DEM resolution is interpolated to a 2 m grid and derived from ~150 images taken during an overflight using a DJI Mavic Pro quadcopter. Visibility to the bottom of the crater was unobstructed during the aerial overflights providing for a map of the entire crater.

The FDTD code, *InfraFDTD*, developed by Kim & Lees (2014), implements a source located at the lava lake at the bottom of the DEM's crater. The model solves the acoustic wave equation over a 3-dimensional topographic domain and is widely used in a variety of previous volcanic studies (Kim & Lees, 2011; Kim et al., 2012; Lacanna & Ripepe, 2013). Although the code does not permit an advecting (windy) atmosphere, it does allow vertically varying sound speed structures, user-specified DEMs, and user-selected source-time functions. *InfraFDTD* uses a perfectly matched layer absorbing boundary condition at the computational domain boundaries and a perfectly reflecting boundary on the topographic surfaces; in my experience, the absorbing boundary condition performed well and did not permit any significant reflections or artifacts from the model boundaries.

InfraFDTD is an incredibly robust 3D model which requires powerful processing units and a high-resolution DEM. This complex model has certain advantages and drawbacks when compared to a simpler model. Watson et al. (2019) demonstrated how a quasi-1D model (CRes), which requires significantly less processing power, is just as efficient in solving for Green's Functions and inverting for axisymmetric crater shapes as a 3D model. Although, for non-axisymmetric crater shapes or in-depth analysis of spatial

frequency variations, the 1-D model would fall short. In addition, topography outside of the crater, which may affect acoustic signals, is often too complex to be approximated within the 1D model. Because this study is focusing on spatial frequency variations as well as second order influences on infrasound signal's frequency, the 3D InfraFDTD model is appropriate and necessary.

Model runs are made on a Graphics Processing Unit (GPU) from the R2 high performance computer cluster at Boise State, which can parallelize the FDTD calculations for fast model runs, permitting many tests. Our standard model run, which involves 250 x 250 x 500 grid nodes with 2-meter spacing (corresponding to the mapped region in Figure 2.1) and 2000 time steps (corresponding to 0.0025s intervals, 5 s total), takes about four minutes to run on our cluster. High frequency waves can be simulated without artificial scattering and dispersion in this grid spacing by using at least 10 points per wavelength (Wang, 1996). Kim and Lees (2011) use 20 points per wavelength to suppress numerical dispersion, which sets our maximum frequency at 20 Hz, well higher than the frequency band in question. InfraFDTD models were run many times to help understand the effect of a variety of parameters including source-time function, station location, and homogeneous sound speed. Synthetic waveform outputs are calculated at specific locations corresponding to sensor positions (see Figure 2.1).

Source time functions at the lava lake surface are provided as volumetric flow time series and are provided with different frequency content to compute Villarrica's crater response, or transfer functions (such as described by Johnson et al. in 2018b and Watson et al. in 2020). The source inputs include Blackman-Harris functions (Harris, 1978) ranging from 0.7-2.5 Hz as well as a band-pass filtered (0.55-5 Hz) impulse.

Blackman-Harris acoustic source functions are convenient band-limited short-duration time series signals, which are regularly used to represent mass-flux outputs (Kim & Lees, 2011; 2014). The specified corner frequency of the Blackman-Harris represents the high cut corner and may be raised/lowered to decrease/increase the time duration of the source pulse. Figure 2.3 shows examples of Blackman-Harris functions of 1.5 and 2.5 Hz and synthetic waveform outputs for atmospheric sound speeds fixed at 350 m/s.

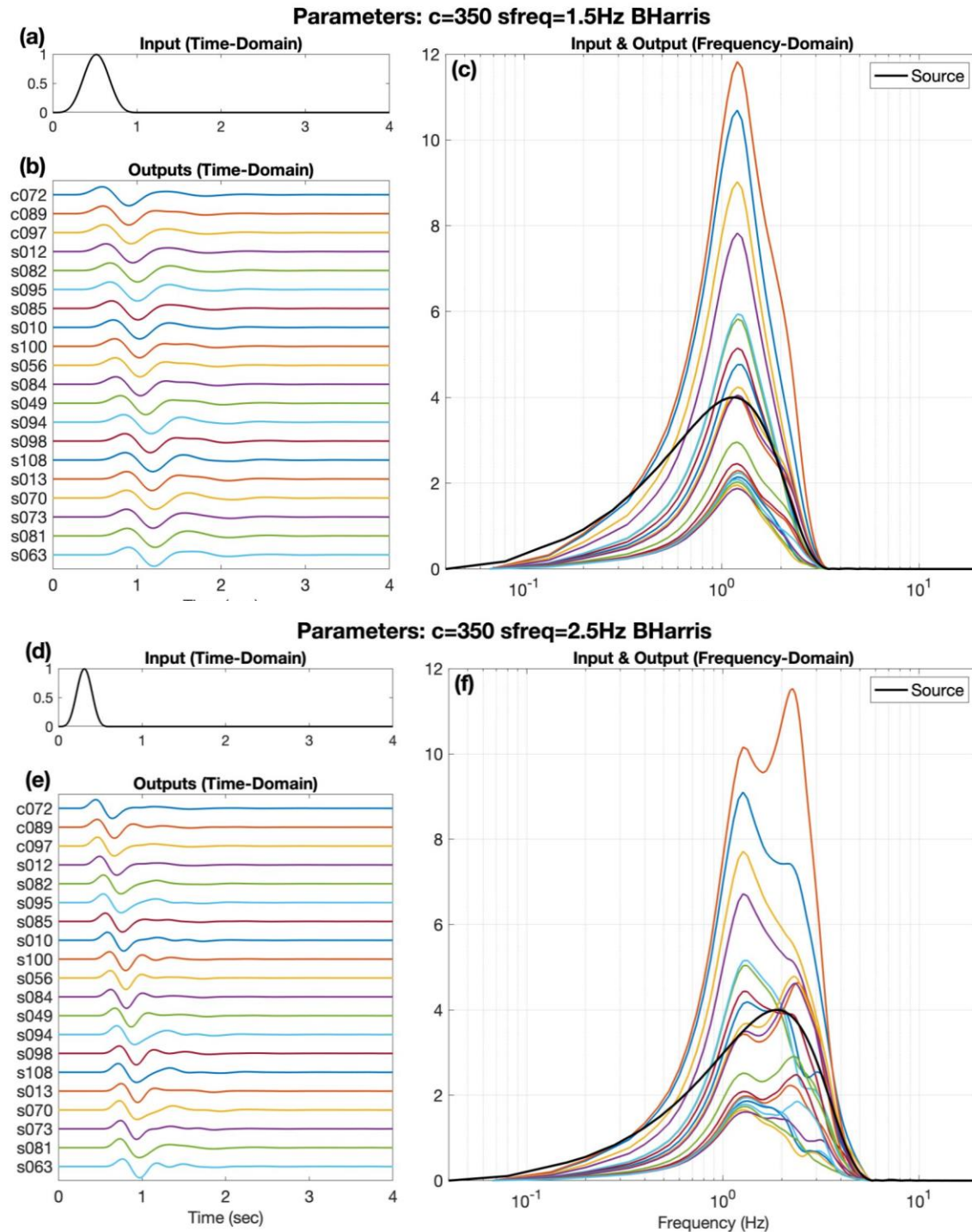


Figure 2.3 Examples of two model runs with 350 m/s sound speed and a Blackman-Harris volumetric flow source function (a) at 1.5 Hz and (d) at 2.5 Hz. (b, e) Normalized synthetic signals at the sensor positions shown as receiver gathers. (c, f) Spectra of synthetic signals for all stations along with source input frequency spectrum (black curve).

2.3 Spectral Analysis

To quantify the peak spectral distribution of Villarrica's infrasound recorded at the summit, histograms were calculated from each station's spectral peak values for a full day recording period. Peak frequencies are calculated for 100 s (10000 sample) Hamming windows with 50% overlap (see Figure 2.4 for distributions from six stations).

Histograms are Gaussian shaped for stations located within the crater and on the cable (e.g., s010, s012, s084, c097) whereas s094 and s100 (on or outside the crater rim) show a second peak frequency at ~ 0.5 Hz due presumably to occasional time windows when microbarom peaks were more pronounced than volcanic tremor peaks. This Gaussian shaped peak frequency distribution curve is unsurprising due to the nature of Villarrica's monotonic resonant infrasound and the fact that it's in a background state. Villarrica's resonance wavers somewhat randomly around a central, resonant peak frequency, with lower probability associated with the greater variations. The stations outside of or on the crater's rim, which have a worse signal-to-noise ratio, do not fit this Gaussian shaped curve.

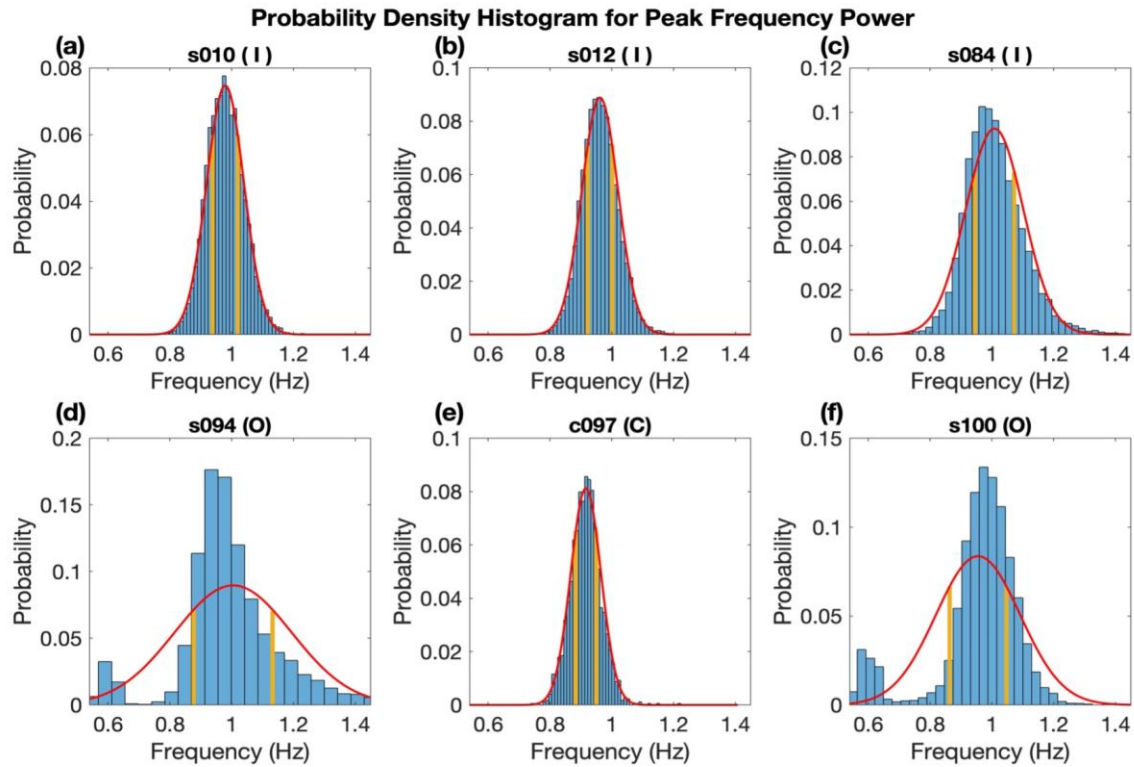


Figure 2.4 (a)-(f) Day-long histograms of peak frequencies for six different stations and best-fit normal distribution (red trace) showing 25th and 75th percentiles (yellow bars). Peak frequencies are calculated with 100 second windows and 50% overlap, resulting in ~1,700 windows grouped into 50 bins.

CHAPTER THREE: RESULTS AND DISCUSSION

3.1 Spatial and Temporal Frequency Fluctuations

Data recorded by the network show both temporal and spatial variations in peak frequency, although more variation is observed temporally. In other words, spectral peak values appear to reflect source controls as opposed to propagation controls. For a given station, temporal variations in peak frequency have been found up to $\pm 17\%$ (e.g., 0.8 to 1.2 Hz; Figure 2.4; Figure 3.1). Spatially, frequency variations across stations are more limited, and deviate by only about $\pm 10\%$ (e.g., ± 0.1 Hz, Figure 3.2, Figure 3.3a). These temporal and spatial variations are shown clearly in Figure 3.3a, such as at seconds 350-400, where the mean peak frequency values shift up ~ 0.15 Hz ($+ \sim 17\%$) but the total spatial variability ranges only ~ 0.05 Hz ($\pm \sim 3\%$). There are a few exceptions to this, such as at second 550 or 900 (Figure 3.3a), where the signal-to-noise ratio decreases, and ambient noise overpowers a lower amplitude tremor (Figure 3.3b). This result implies that an infrasound recording anywhere at the top of the volcano (inside or outside the crater) will detect temporal changes of frequency characteristics reliably.

An investigation over whether a possible diurnal cycle might influence the frequency distributions is performed by computing frequency statistics for day and night time bins (Figure 3.4). The initial assumption made considers that lower night time temperatures in the crater might lower the intrinsic sound speed, which would result in lower frequencies. Because no patterned day-to-night variation in recorded infrasound frequency was observed, it's concluded that frequency excursions are not principally due

to ambient atmospheric conditions. This finding does not prove that there is no major influence from the ambient atmospheric conditions, but it does indicate this result.

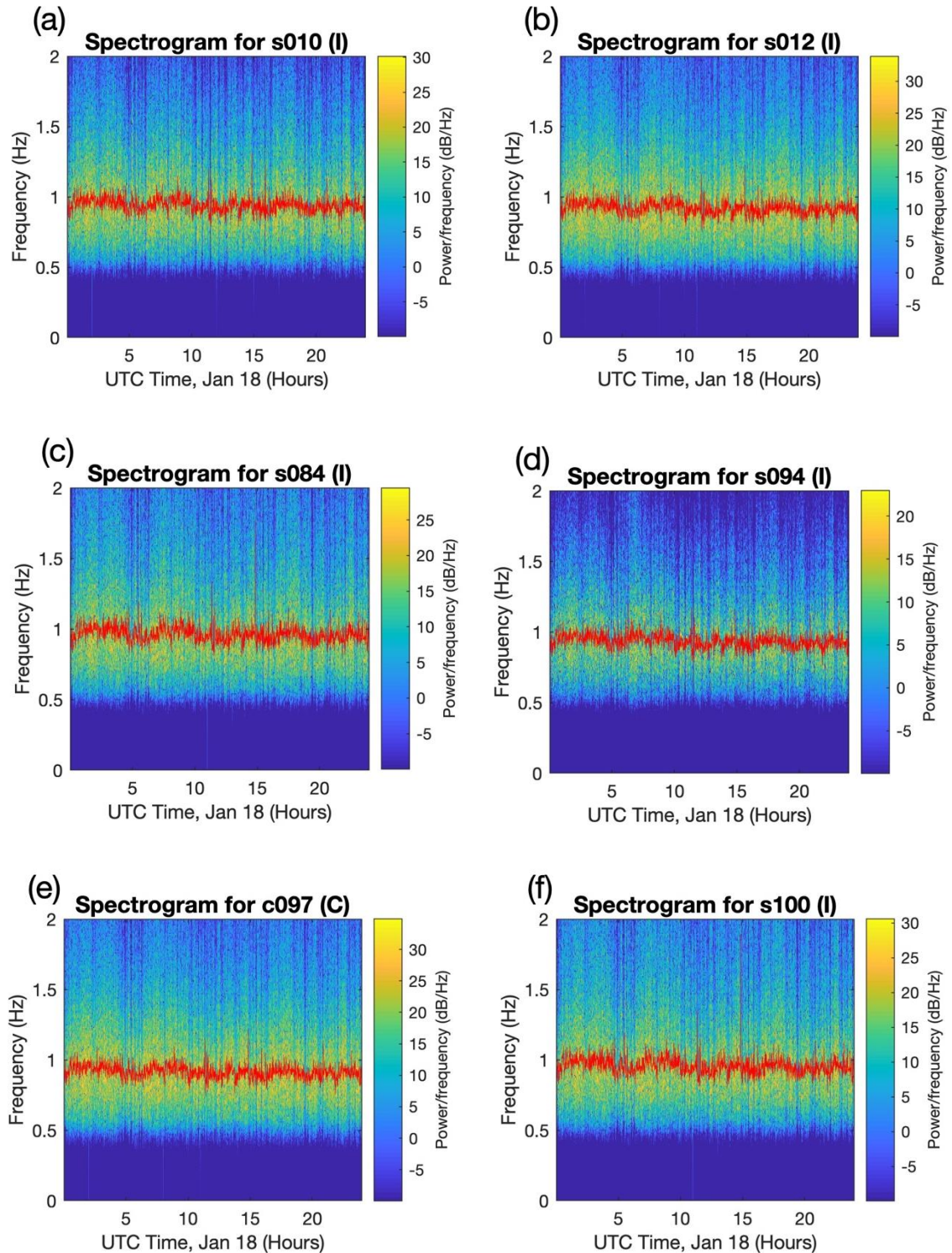


Figure 3.1 (a)-(f) Day-long spectrograms from January 18, 2020, for the 6 stations indicated in Figure 2.4. The peak amplitude frequency has been indicated with a red line. Window duration is 100 s with 50% overlap. Spectral content has been filtered above a 0.55 Hz corner.

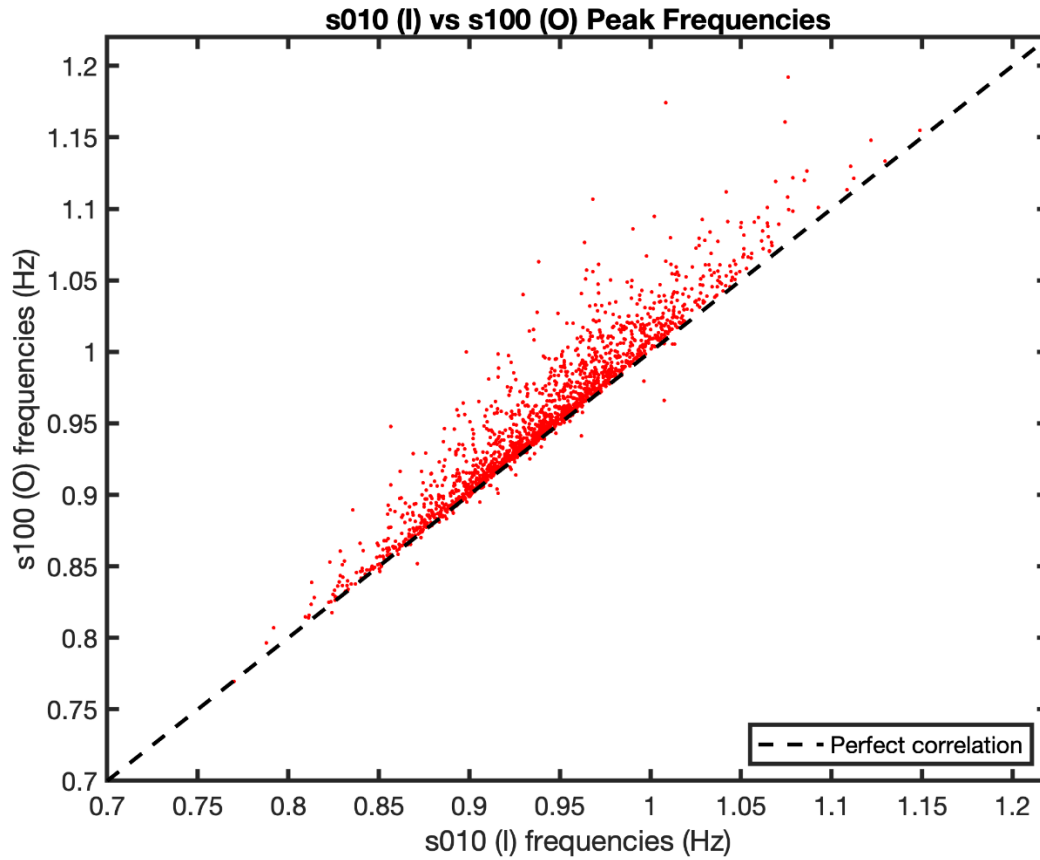


Figure 3.2 X-Y scatter plot comparing the peak frequencies recorded from station s010 (I) and s100 (O). The dashed black line indicates where the perfect correlation between sensors is.

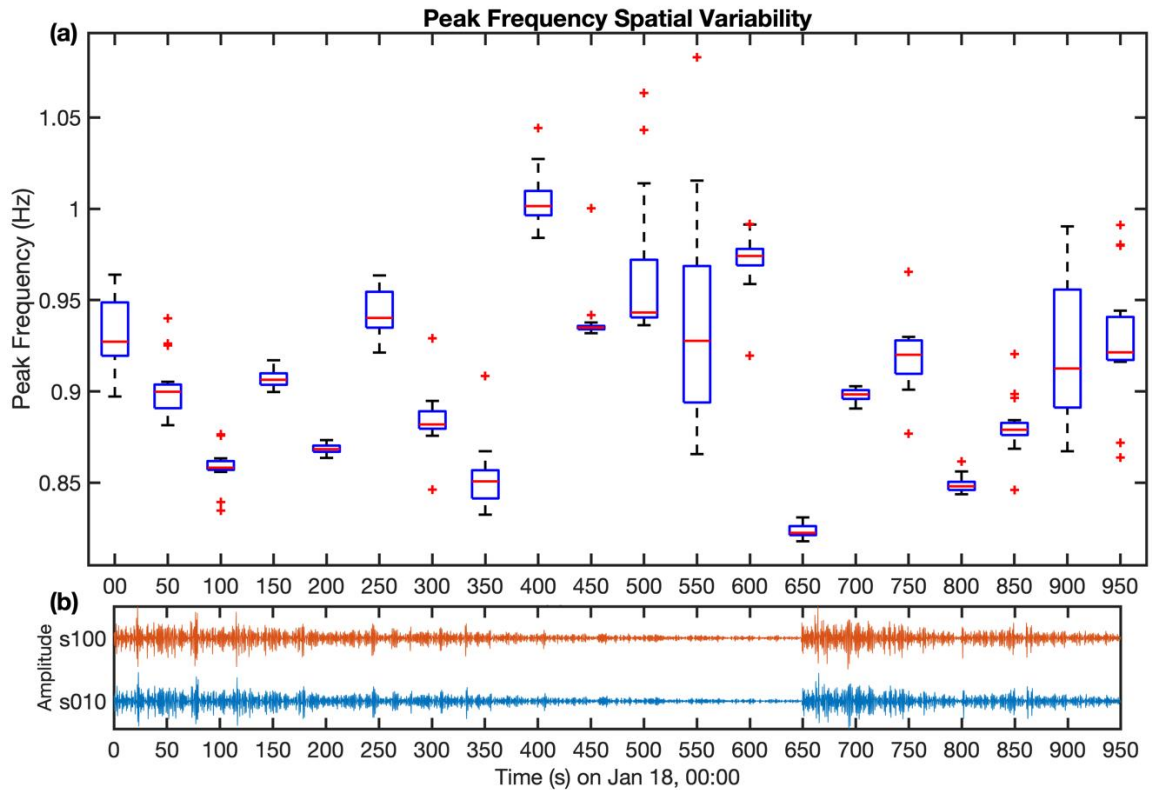


Figure 3.3 (a) Box-and-whisker spatial peak frequency plot. Each box contains twenty peak frequency values (one per station) for a 100 s window. The window is then advanced by 50 s (50%) and recalculated. Box limits correspond to 25 and 75 percentiles and whiskers encapsulate 95% of data. (b) Time-series record (band-pass filtered between .55 and 5 Hz) from s010 (I) and s100 (O) showing the variations in infrasound tremor amplitude.

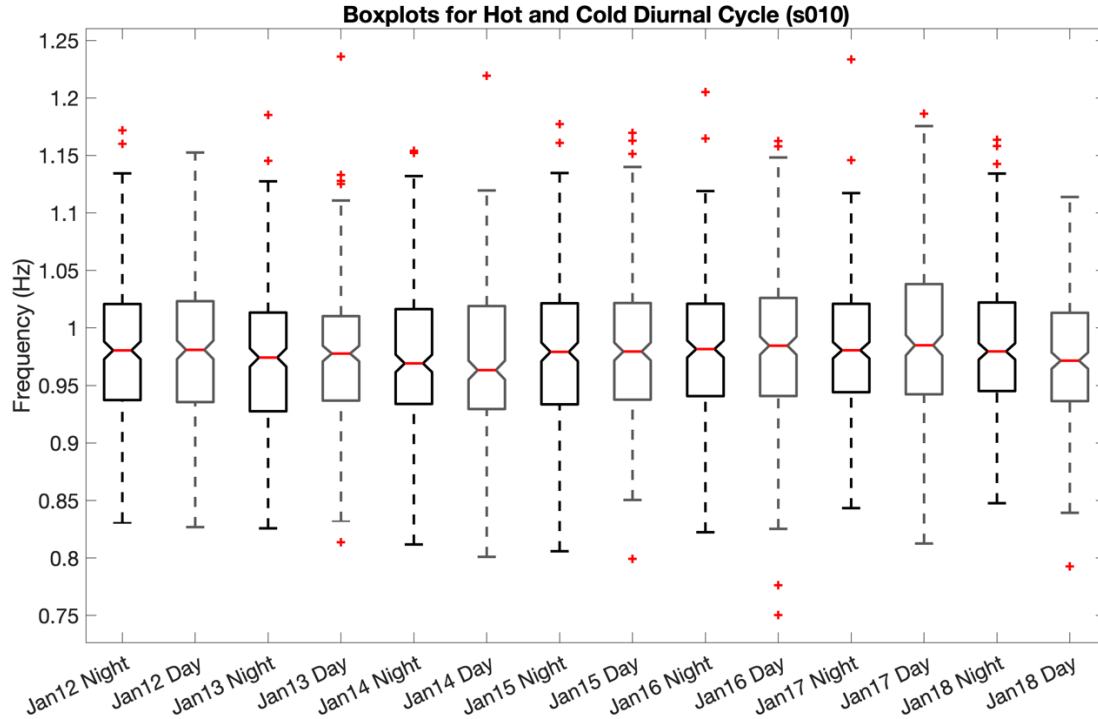


Figure 3.4 Box-and-whisker peak frequency plot for s010 (O) during the four coldest hours of the night (0:00-4:00, local time, black) and the four hottest hours of the day (11:00-15:00, local time, gray) for the week-long dataset. Box limits correspond to 25 and 75 percentiles and whiskers encapsulate 95% of data. Peak frequencies are calculated from spectrograms as in Figure 2.4 using 100 s windows and 50% overlap.

3.2 InfraFDTD Outputs

Synthetic waveform spectra calculated by InfraFDTD are compared with recorded infrasound spectra to elucidate the source spectrum of infrasound produced by Villarrica assuming a source affixed to the lava lake at the bottom of the crater. InfraFDTD models were run with an assortment of Blackman-Harris source-time functions (of varying frequencies) in an attempt to *forward-match* a source spectrum's synthetic output to observed data. At this point only the spectral components are investigated and there are no attempts to invert for amplitudes of source functions.

Models are run with a range of homogeneous sound speeds using various Blackman-Harris wavelets. The InfraFDTD model produces multiple synthetic pressure

time series for which peak spectral frequency is calculated. Synthetic spectra are affected both by the acoustic response of the crater (determined by sound speed) and by the source function. Figure 3.5 shows trends relating Blackman-Harris source frequency and sound speed to peak output frequency. For example, for a given output frequency of 1.0 Hz, the input corner for the Blackman-Harris is 0.9 Hz at 400 m/s, 0.975 Hz at 350 m/s, and 1.3 Hz at 300 m/s.

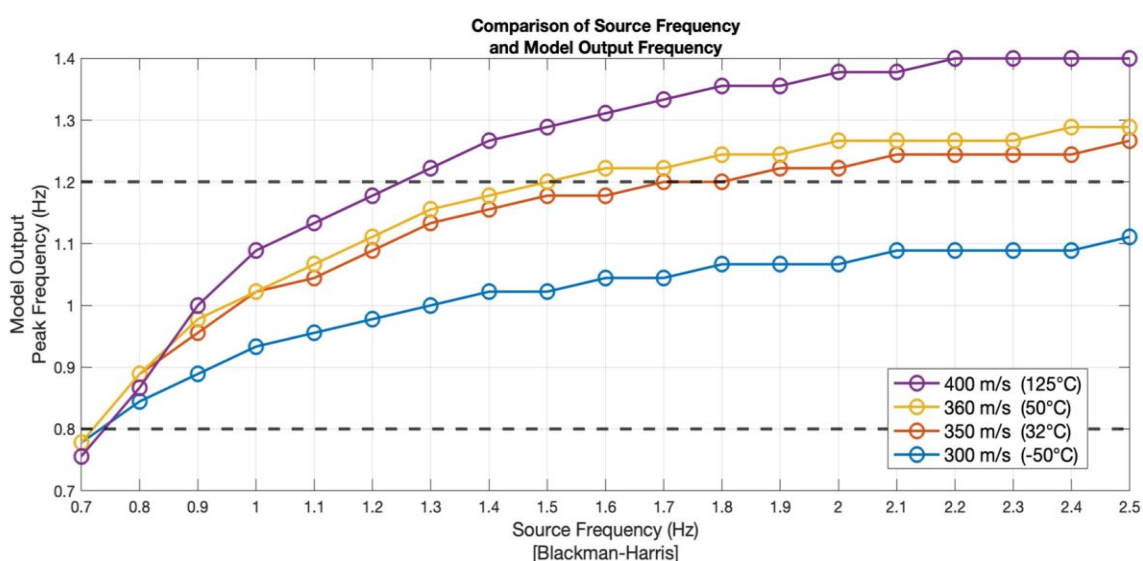


Figure 3.5 Relationship between input Blackman-Harris source frequency (x-axis) and modeled peak frequency (y-axis) for a range of crater sound speeds. All model runs used a Blackman-Harris source function as an input. Dashed horizontal lines correspond to the range of peak frequencies recorded.

3.2.1 Sound Speed

Adiabatic non-advecting sound speed is primarily a function of molar mass and temperature (Pierce, 2019). The assumption here, that the crater is primarily composed of standard atmosphere ($\sim 78\%$ N_2 and $\sim 21\%$ O_2), follows Shinohara & Witter (2005) who reported that each plume ejection at Villarrica, which was made up of up to 95% H_2O and much lower concentrations of CO_2 and sulphur species, accounted cumulatively for

only 1% of the total crater atmosphere. In addition, observations during the field expedition indicated clear visibility into and across the crater (i.e., limited condensed volcanic steam) as well as nonhazardous air quality conditions for tourists. Therefore, the assumption of a standard atmospheric molar mass is appropriate, e.g., $c = \sqrt{\gamma RT}$, where the specific gas constant $R = \sim 287 \text{ J/kg/K}$ (dry air) and gamma (γ) = 1.4, and only consider the effects of temperature (T) variations. To address any skepticisms towards this approach, we calculate the resulting change in sound speed (as a function of temperature) using the reported values of Villarrica's plume injections. With water vapor (H_2O) being the most prevalent gas within Villarrica's plume, we find that the molar mass changes from 28.95 g/mol to 28.41g/mol with up to 5% water vapor (4% greater than reported). This new approach changes the sound speed from 20.05T to 20.24T, a variation of less than 1%.

The Gem loggers' internal temperature sensors, including those suspended on the cable less than 100 m from the lava lake, ranged from 4-28 °C corresponding to sound speeds ranging 330-350 m/s. Such temperatures were less than those estimated by Goto & Johnson in 2011 (during a more active period of lava lake convection) and where the temperature probably exceeded 100 °C. Although the temperature distribution within Villarrica's crater is spatially variable, Watson et al. (2019) shows the limited influence of a linearly changing temperature and affirmed that a constant temperature value averaged throughout the crater volume could provide reasonable model estimation.

3.3 Villarrica's Infrasonic Sources

3.3.1 The Continuous Infrasonic source

Given that the limits over the peak frequency values for most of the recorded data are between 0.8 and 1.2 Hz, these results suggest that the primary infrasonic source process must be lower than about 1.4 Hz (from Figure 3.5). Higher frequency Blackman-Harris sources can yield 0.8 to 1.2 Hz outputs, but only for unrealistically low sound speeds in the crater (300 m/s corresponds to -50 degrees C; see blue trace).

For more reasonable crater sound speeds exceeding 350 m/s ($> \sim 32^{\circ}\text{C}$), the excursions in frequency content can be explained by source frequency variations rather than by sporadic changes in temperature caused by emission of hot gas filling or partially filling the crater. It is possible that unsteady degassing from the lava lake occasionally perturbs the average temperature of the crater to values of about 50 degrees C (360 m/s), but it is unlikely that temperatures rose much higher during our experiment. To observe peak frequencies ranging ± 0.2 Hz, it is most probable that a variable source is responsible. As mentioned previously, these excursions in the data are not explainable by diurnal variations.

3.3.2 The Impulsive Infrasonic Source

The persistent lava lake degassing and/or surface convection, coupled with the Villarrica's unique crater acoustic response, is responsible for the bulk of the 0.8 to 1.2 Hz tremor that has been noted in this and many previous studies over the years (Goto & Johnson, 2011; Johnson et al., 2018b; Richardson & Waite, 2013; Richardson et al., 2014; Ripepe et al., 2010; Watson et al., 2019). However, during our 2020 field work, rare exceptions were noted when higher frequency modes were excited by small

explosions from the lava lake. Spatter bursts and small Strombolian eruptions occurred approximately hourly and triggered energy peaks at or above about 5 Hz. Given that these were short duration transients, they are most easily seen on spectrograms with short windows (Figure 3.6) in which energy above 5 Hz is evident on the summit infrasound stations.

These small Strombolian eruptions at Villarrica are impulsive in nature and thus have a source spectrum that is relatively broadband. To replicate the crater acoustic spectrum associated with these short spatter bursts, synthetics are produced for an impulse based on a delta function band-passed between 0.55 and 5 Hz (Figure 3.7). Notably, a higher (>5 Hz) mode is evident in the synthetic output source from an impulse. The higher frequency spectral peak is much more variable across the network of sensors around the crater rim, showing that higher frequency spectral energy depends strongly upon station location.

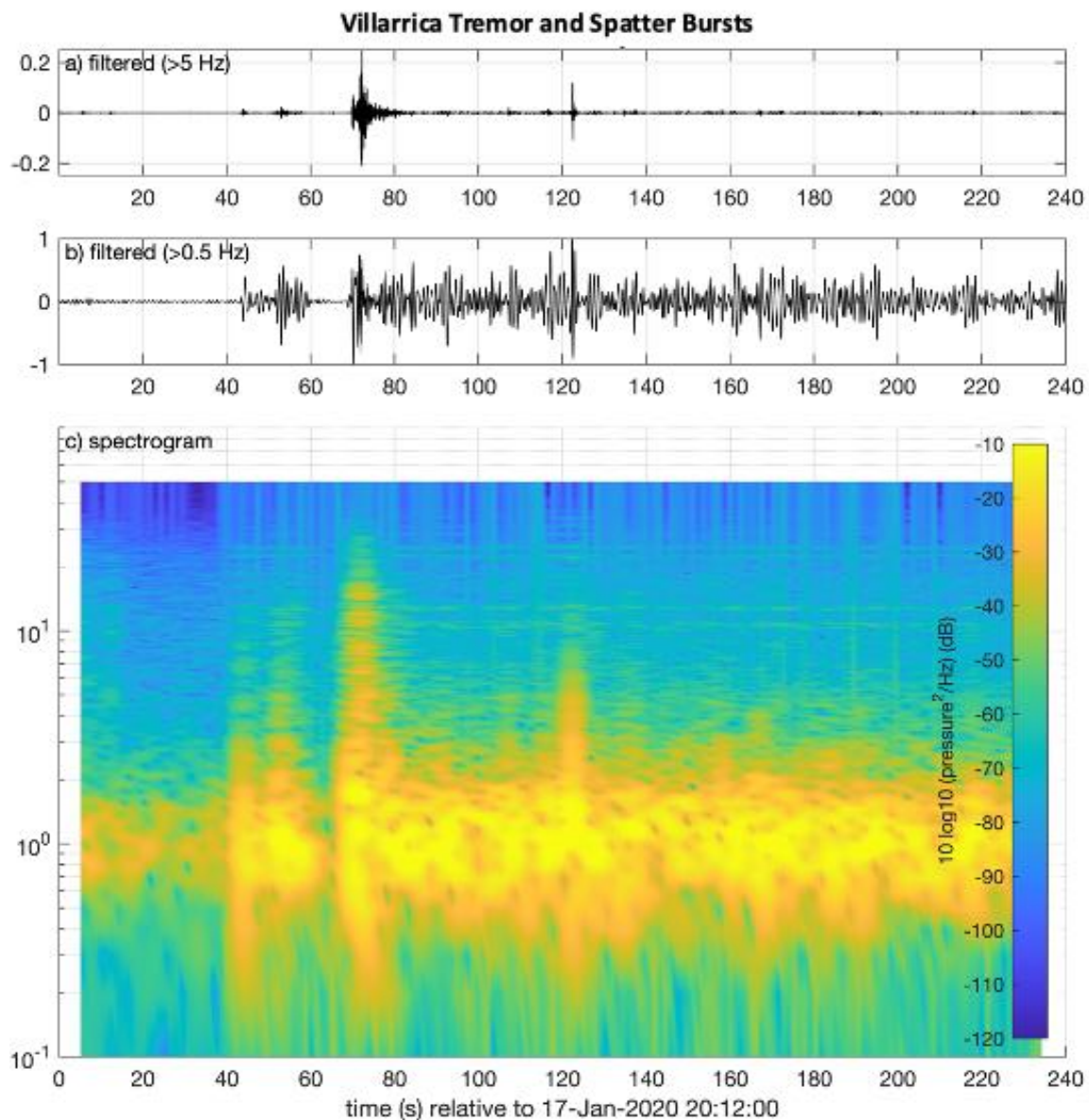


Figure 3.6 Station s108 infrasound time-series and spectrogram associated with three small spattering/Strombolian events. a) 5 Hz high-pass filtered time-series showing significant energy above 5 Hz. b) 0.5 Hz high-pass filtered time series showing prevalent background tremor and high frequency components largely obscured. c) Spectrogram of the 0.5 Hz high-passed data calculated for 10 s intervals and 50% overlap.

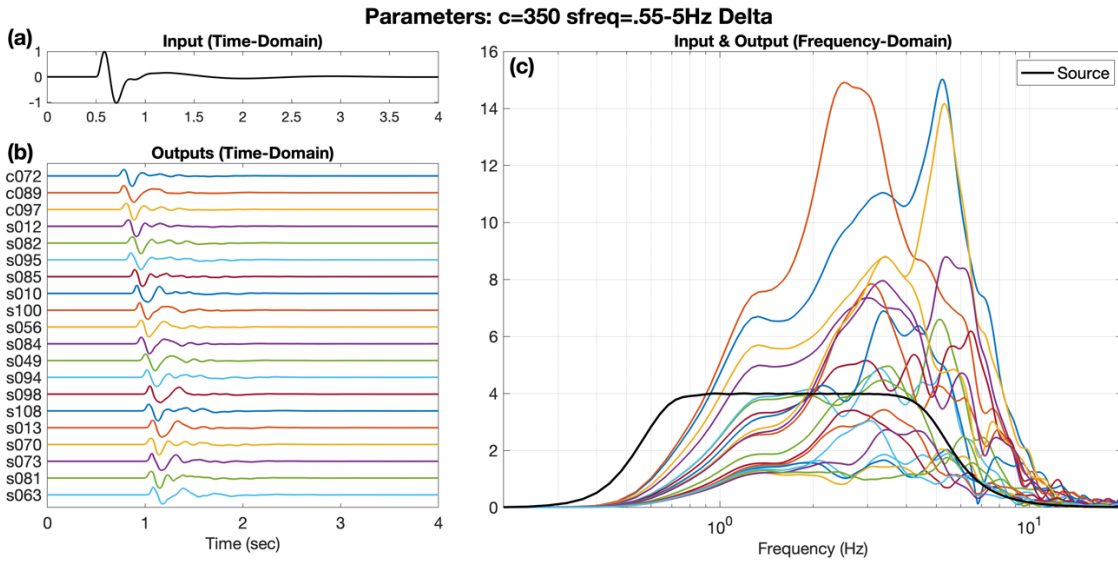


Figure 3.7 Impulse source-time function and modeled time series and spectra with 350 m/s sound speed. (a) Modeled Dirac delta pressure function band-pass filtered with 4 poles between 0.55 and 5 Hz. (b) Synthetic output for the distributions of sensors deployed at Villarrica. (c) Output amplitude spectra. The black curve indicates the source-time function spectrum.

3.3.3 Interpretation of the Infrasonic Sources

Two types of source time functions for Villarrica's infrasonic production are identified and attempted to be model (Figure 3.8). During the 2020 field campaign, Villarrica's Strombolian eruptions were much smaller than the 0.7-1 Hz explosions described in Johnson et al. (2018b) leading up to the 3 March 2015 paroxysm. The small explosions in 2020 were also much shorter in duration, which is why dominant frequencies in these signals were as high as 5 Hz and with relatively low amplitudes often obscured by the more intense ~ 1 Hz background tremor.

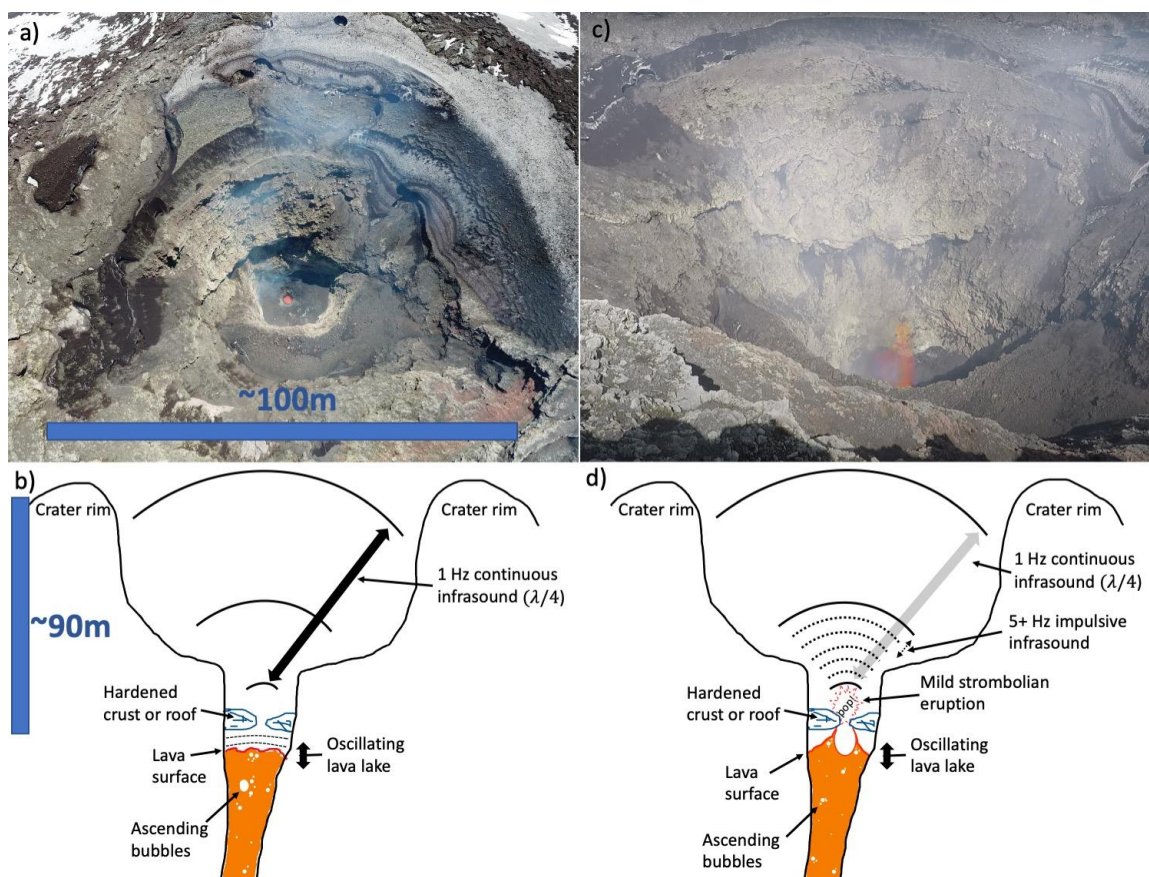


Figure 3.8 Images of Villarrica's crater and schematic interpretation of geometry and sound wavelengths. a) UAV-based photograph of the inside of Villarrica's crater taken on 15 January 2020 and showing a lava lake skylight as described by Palma et al. (2008) and Goto & Johnson (2011). b) Schematic cross section of the crater highlighting the continuous infrasound excited by movement of/from the lava lake. c) Image from crater rim showing a small Strombolian eruption on 16 January 2020. d) Schematic cross section of the crater during Strombolian activity showing 5 Hz infrasound wavelengths drawn approximately to scale.

3.4 Synthetic Infrasound Source-Time Function

To better understand the source of Villarrica's continuous infrasound, synthetically derived Green's functions are deconvolved from the recorded data in the frequency domain. Using the band-pass filtered impulse response highlighted in Figure 3.7, the source spectrum is assumed to be valid within the frequency range of 0.55 to 5 Hz assuming a constant Green's function and therefore linear time invariance (Riad, 1986). Source spectra solutions are calculated for each station by dividing its tremor

spectrum by the synthetic Green's function for that station. Figure 3.9 shows the workflow for deconvolution and source spectra recovery.

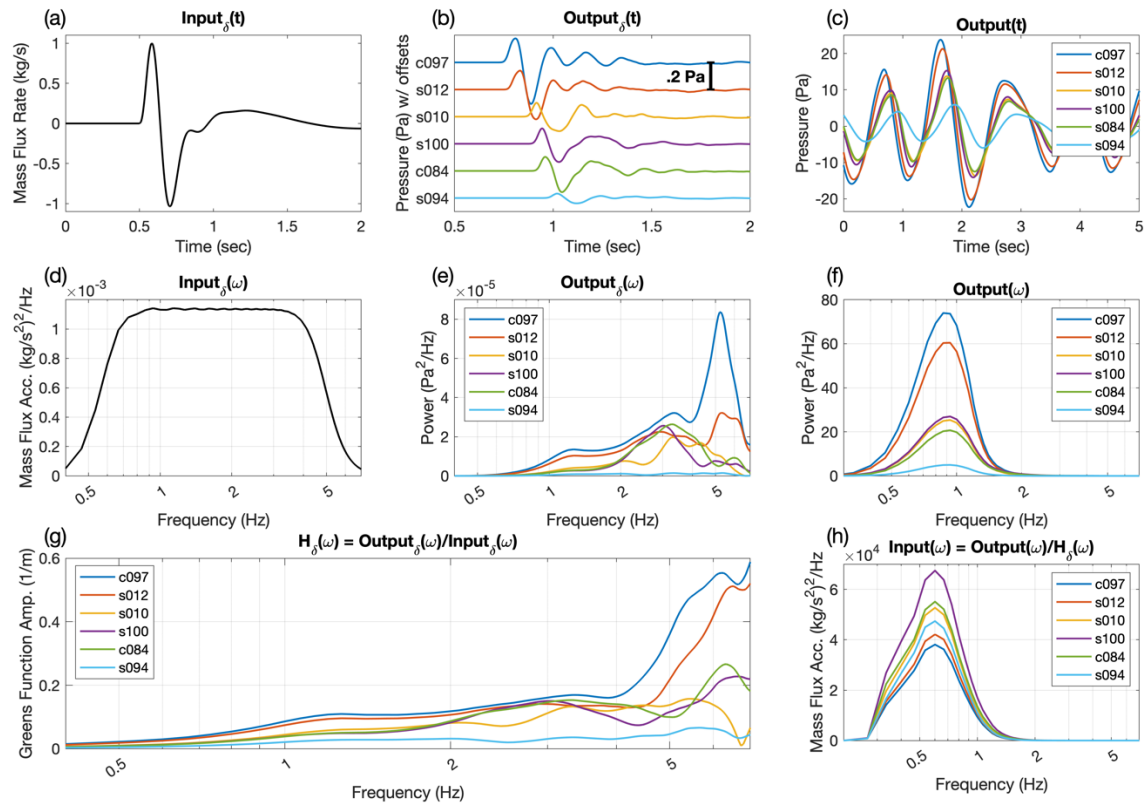


Figure 3.9 Deconvolution of crater acoustic response from tremor examples at 6 stations. (a) Band-passed impulse from Figure 3.7a. (b) Impulse response calculated for several stations from Figure 3.7b. (c) Tremor examples recorded at several stations from 18 January. (d, e, f) Spectra from panels a, b, c respectively. (g) Green's functions for each station. (h) Deconvolved source inputs for each station from spectral division of recorded infrasound divided by Green's functions.

With the assumption of a linear time invariance, the theoretical sources (Figure 3.9h) are expected to match perfectly, yet their amplitudes differ by as much as a factor of two. This can be attributed to several minor influences within InfraFDTD such as the resolution of the DEM (2 meters), rounded sensor placement on the modelled grid space, the use of a homogenous atmospheric sound speed, and to a lesser extent, the non-advecting modelled atmosphere. Since the amplitudes are within an order of magnitude

from each other and the shape is consistent for the different station's sources, this indicates that the source location assumption (bottom of crater/top of lava lake) and InfraFDTD modeling outputs give believable results. This consistent source shape result does not prove that the methods of this study are sound, but it does support that idea.

CHAPTER FOUR: IMPLICATIONS AND CONCLUSION

4.1 The Implications

As stated previously, one of the primary goals of volcanology is eruption forecasting and hazard mitigation. This study aims to improve upon the communal collection of knowledge involving not just Villarrica, but other similar, open-vent volcanoes in regard to these primary goals. Forecasting efforts require the identification of patterns from past behaviors. Since the practice of volcano acoustics is relatively young, there is plenty to gain through observing and analyzing these systems' acoustic signals.

4.1.1 Importance

There is great importance and significance behind assessing the background state of Villarrica (and other similar volcanoes). In specific regards to Villarrica, it is one of the most active volcanoes in Chile with a booming tourist industry and a dense local population surrounding it. To make matters worse, the summit is glaciated and poses risk of lahar hazards. In 2015, Villarrica erupted violently with lava fountains reaching heights of 1.5 km into the air (Romero et al., 2018). The local population was evacuated and tourism to the area was halted. As a result, there were major monetary losses, water shortages, and plenty of inconveniences for thousands of people. Thankfully, the evacuations were timely and there were no deaths reported directly from the eruption. This paroxysm was handled with a proper assessment of the hazards involved, but that is not always the case. Villarrica is known to erupt about every 10-15 years, so the better we understand the hazards and can forecast the eruptions, the more prepared we will be for

the next impending eruption. Many of these points are applicable to other volcanoes of similar nature. Information pertaining to one specific volcano can often be useful when considering other systems. Most active volcanos in the world will erupt violently multiple times. The specific hazards of each system may vary, but the overall importance of understanding these systems and their hazards is consistent across all volcanos.

4.1.2 Limitations

There are a few limits to this study worth mentioning. To begin, no temperature or gas composition measurements were made during the time of infrasound collection. This study has used the indirect, internal temperature of the GEM sensors and gas composition values from previous studies. While these assumptions were introduced and implemented appropriately, they subsequently limit the ability to investigate either of these properties in depth. Thus, we approached the topic of sound speeds as a function of temperature only within a homogeneous atmosphere. Clearly, temperature profile within the crater of Villarrica is not truly homogenous, but we consider the result from Watson et al. (2019) which has shown the limited influence of a linearly changing temperature.

Another major limit to this study was the absence a video record that had a line of sight of Villarrica's lava lake level during the collection period. Since the lava lake level was so low during this time, it could not be seen directly from most access points. Thus, it is assumed that the lava lake level remained the same as it was during our one drone flyover (another minor limitation). This assumption is also supported by reports from the Observatorio Volcanológico de los Andes del Sur (OVDAS) where no change in the lava lake level was indicated (Global Volcanism Program, 2020).

Lastly, this study only spanned a week's worth of time where infrasound data was collected. While this was an adequate amount of time for the methods and analysis of this study, it still limits the sample size for analysis and allows no room for long-term assessment of Villarrica's frequency excursion.

4.1.3 Future Work

There are a few directions this work can progress. Since this study spanned a one-week period in January 2020, it would be useful to investigate other one-week periods where Villarrica is in a background state. This would help refine any knowledge concerning Villarrica during background states while also building off of and developing a catalog of what to expect during volcanic background states in general. Ideally, placing the sensors in a similar location will allow for a direct comparison between the data recorded. This study could also be replicated on a different but similar open-vent volcano such as Mount Nyiragongo (Democratic Republic of Congo), Kilauea (Hawaii), Mount Etna (Italy), and others. This would allow for a direct comparison of these various volcanos' background states. With enough investigation over multiple systems, specific similarities and differences between each system can be drawn and thus investigated.

4.2 Conclusion

Villarrica is a classic example of an open-vent volcano producing continuous infrasonic tremor with a peaked spectrum, sourced by an actively convecting lava lake deep within a resonating horn-shaped crater. This study quantifies the dominant spectral peak at Villarrica and its variability over time and space using a network of twenty infrasonic microphones around and within the crater rim, including three suspended over the lava lake on a cable. Signals recorded continuously over one week showed that

although a low frequency 1 Hz tremor exhibited excursions of up to ± 0.2 Hz ($\pm 17\%$), when excursions did occur, all sensors across the crater detected it. Since a rise in Villarrica's frequency content may be a precursor to paroxysms (Johnson et al. 2018b), the variability of this frequency content is of major importance in terms of monitoring and forecasting eruption at Villarrica. The up to ± 0.2 Hz excursions are noted as being somewhat random due to the shape of the peak frequency distributions and cannot be easily explained via realistic fluctuations in crater sound speed (either due to emissions of hot gas or diurnal temperature fluctuations). Therefore, variations in source spectral content are the most likely cause.

This study has also identified two independent sources for Villarrica's infrasound production (one continuous and one discrete). The continuous signal is resonant in nature with a peaked spectra, while the discrete signal involves a broadband, higher amplitude signal that is relatively short lived. The efforts from the InfraFDTD model support these findings as well as the data recorded and constrain the values of reasonable parameters such as sound speed and source frequency while also approximating the frequency content for the source of Villarrica's continuous infrasound.

REFERENCES

- Allstadt, K. E., Matoza, R. S., Lockhart, A. B., Moran, S. C., Caplan-Auerbach, J., Haney, M. M., Thelen, W. A., & Malone, S. D. (2018). Seismic and acoustic signatures of surficial mass movements at volcanoes. *Journal of Volcanology and Geothermal Research*, 364, 76–106.
<https://doi.org/10.1016/j.jvolgeores.2018.09.007>
- Anderson, J. F., Johnson, J. B., Bowman, D. C., & Ronan, T. J. (2018). The Gem Infrasound Logger and Custom-Built Instrumentation. *Seismological Research Letters*, 89(1), 153–164. <https://doi.org/10.1785/0220170067>
- Dzierma, Y., & Wehrmann, H. (2010). Eruption time series statistically examined: Probabilities of future eruptions at Villarrica and Llaima Volcanoes, Southern Volcanic Zone, Chile. *Journal of Volcanology and Geothermal Research*, 193(1–2), 82–92. <https://doi.org/10.1016/j.jvolgeores.2010.03.009>
- De Angelis, S., Fee, D., Haney, M., & Schneider, D. (2012). Detecting hidden volcanic explosions from Mt. Cleveland Volcano, Alaska with infrasound and ground-coupled airwaves. *Geophysical Research Letters*, 39(21), 1–6.
<https://doi.org/10.1029/2012GL053635>
- Fee, D., Garcés, M., Patrick, M., Chouet, B., Dawson, P., & Swanson, D. (2010). Infrasonic harmonic tremor and degassing bursts from Halema'uma'u Crater, Kilauea Volcano, Hawaii. *Journal of Geophysical Research: Solid Earth*, 115(11), 1–15. <https://doi.org/10.1029/2010JB007642>
- Fee, D., Haney, M. M., Matoza, R. S., Van Eaton, A. R., Cervelli, P., Schneider, D. J., & Iezzi, A. M. (2017). Volcanic tremor and plume height hysteresis from Pavlof Volcano, Alaska. *Science*, 355(6320), 45–48.
<https://doi.org/10.1126/science.aah6108>

- Harris, F. J. (1978). On the Use of Windows for Harmonic Analysis with the Discrete Fourier Transform. *Proceedings of the IEEE*, 66(1), 51–83.
<https://doi.org/10.1109/PROC.1978.10837>
- Global Volcanism Program, 2020. Report on Villarrica (Chile). In: Sennert, S K (ed.), Weekly Volcanic Activity Report, 22 January-28 January 2020. Smithsonian Institution and US Geological Survey.
- Goto, A., & Johnson, J. B. (2011). Monotonic infrasound and Helmholtz resonance at Volcan Villarrica (Chile). *Geophysical Research Letters*, 38(6), 1–5.
<https://doi.org/10.1029/2011GL046858>
- Gurioli, L., Harris, A. J. L., Houghton, B. F., Polacci, M., & Ripepe, M. (2008). Textural and geophysical characterization of explosive basaltic activity at Villarrica volcano. *Journal of Geophysical Research: Solid Earth*, 113(8), 1–16.
<https://doi.org/10.1029/2007JB005328>
- Johnson, J. B., & Palma, J. L. (2015). Lahar infrasound associated with Volcán Villarrica's 3 March 2015 eruption. *Geophysical Research Letters*, 42(15), 6324–6331. <https://doi.org/10.1002/2015GL065024>
- Johnson, J. B., Ruiz, M. C., Ortiz, H. D., Watson, L. M., Viracucha, G., Ramon, P., & Almeida, M. (2018a). Infrasound Tornillos Produced by Volcán Cotopaxi's Deep Crater. *Geophysical Research Letters*, 1–9.
<https://doi.org/10.1029/2018GL077766>
- Johnson, J., & Watson, L. (2019). Monitoring Volcanic Craters with Infrasound “Music.” *Eos*, 100 (March). <https://doi.org/10.1029/2019eo123979>
- Johnson, J. B., Watson, L. M., Palma, J. L., Dunham, E. M., & Anderson, J. F. (2018b). Forecasting the Eruption of an Open-Vent Volcano Using Resonant Infrasound Tones. *Geophysical Research Letters*, 45(5), 2213–2220.
<https://doi.org/10.1002/2017GL076506>
- Kim, K., & Lees, J. M. (2011). Finite-difference time-domain modeling of transient infrasonic wavefields excited by volcanic explosions. *Geophysical Research Letters*, 38(6), 2–6. <https://doi.org/10.1029/2010GL046615>

- Kim, K., Lees, J. M., & Ruiz, M. (2012). Acoustic multipole source model for volcanic explosions and inversion for source parameters. *Geophysical Journal International*, *191*(3), 1192–1204. <https://doi.org/10.1111/j.1365-246X.2012.05696.x>
- Kim, K., & Lees, J. M. (2014). Local volcano infrasound and source localization investigated by 3D simulation. *Seismological Research Letters*, *85*(6), 1177–1186. <https://doi.org/10.1785/0220140029>
- Lacanna, G., & Ripepe, M. (2013). Influence of near-source volcano topography on the acoustic wavefield and implication for source modeling. *Journal of Volcanology and Geothermal Research*, *250*, 9–18. <https://doi.org/10.1016/j.jvolgeores.2012.10.005>
- Lamb, O., Lees, J., Franco Marin, L., Lazo, J., Rivera, A., Shore, M., and Lee, S.: Identifying icequakes at ice-covered volcanoes in Southern Chile, EGU General Assembly 2020, Online, 4–8 May 2020, EGU2020-851, <https://doi.org/10.5194/egusphere-egu2020-851>
- Lyons, J. J., Haney, M. M., Fee, D., Wech, A. G., & Waythomas, C. F. (2019). Infrasound from giant bubbles during explosive submarine eruptions. *Nature Geoscience*, *12*(11), 952–958. <https://doi.org/10.1038/s41561-019-0461-0>
- Marchetti, E., Ripepe, M., Harris, A. J. L., & Delle Donne, D. (2009). Tracing the differences between Vulcanian and Strombolian explosions using infrasonic and thermal radiation energy. *Earth and Planetary Science Letters*, *279*(3–4), 273–281. <https://doi.org/10.1016/j.epsl.2009.01.004>
- Mora-Stock, C., Thorwart, M., Wunderlich, T., Bredemeyer, S., Hansteen, T. H., & Rabbel, W. (2014). Comparison of seismic activity for Llaima and Villarrica volcanoes prior to and after the Maule 2010 earthquake. *International Journal of Earth Sciences*, *103*(7), 2015–2028. <https://doi.org/10.1007/s00531-012-0840-x>
- Naranjo, J. A., & Moreno, H. (2004). Laharic debris-flows from Villarrica Volcano. *Villarrica Volcano (39.5° S), Southern Andes, Chile. Santiago, Servicio Nacional de Geología y Minería*, 28-45.

- Palma, J. L., Calder, E. S., Basualto, D., Blake, S., & Rothery, D. A. (2008). Correlations between SO₂ flux, seismicity, and outgassing activity at the open vent of Villarrica volcano, Chile. *Journal of Geophysical Research: Solid Earth*, *113*(10), 1–23. <https://doi.org/10.1029/2008JB005577>
- Pierce, A. D. (2019). *Acoustics: an introduction to its physical principles and applications*. Springer. p. 28. <https://doi.org/10.1007/978-3-030-11214-1>
- Riad, S. M. (1986). The Deconvolution Problem: An Overview. *Proceedings of the IEEE*, *74*(1), 82–85. <https://doi.org/10.1109/PROC.1986.13407>
- Richardson, J. P., & Waite, G. P. (2013). Waveform inversion of shallow repetitive long period events at Villarrica Volcano, Chile. *Journal of Geophysical Research: Solid Earth*, *118*(9), 4922–4936. <https://doi.org/10.1002/jgrb.50354>
- Richardson, J. P., Waite, G. P., Palma, J. L. (2014). Varying seismic-acoustic properties of the fluctuating lava lake at Villarrica volcano, Chile. *AGU: Journal of Geophysical Research, Solid Earth*, *119*, 3678–3699. <https://doi.org/10.1002/2014JB011002>
- Ripepe, M., Marchetti, E., Bonadonna, C., Harris, A. J. L., Pioli, L., & Ulivieri, G. (2010). Monochromatic infrasonic tremor driven by persistent degassing and convection at Villarrica Volcano, Chile. *Geophysical Research Letters*, *37*(15), 2–7. <https://doi.org/10.1029/2010GL043516>
- Romero, J. E., Vera, F., Polacci, M., Morgavi, D., Arzilli, F., Alam, M. A., Bustillos, J. E., Guevara, A., Johnson, J. B., Palma, J. L., Burton, M., Cuenca, E., & Keller, W. (2018). Tephra From the 3 March 2015 Sustained Column Related to Explosive Lava Fountain Activity at Volcán Villarrica (Chile). *Frontiers in Earth Science*, *6*. <https://doi.org/10.3389/feart.2018.00098>
- Schwaiger, H. F., Lyons, J. J., Iezzi, A. M., Fee, D., & Haney, M. M. (2020). Evolving infrasound detections from Bogoslof volcano, Alaska: insights from atmospheric propagation modeling. *Bulletin of Volcanology*, *82*(3). <https://doi.org/10.1007/s00445-020-1360-3>
- Shinohara, H., & Witter, J. B. (2005). Volcanic gases emitted during mild Strombolian activity of Villarrica volcano, Chile. *Geophysical Research Letters*, *32*(20), 1–5. <https://doi.org/10.1029/2005GL024131>

- Spina, L., Cannata, A., Privitera, E., Vergnolle, S., Ferlito, C., Gresta, S., Montalto, P., & Sciotto, M. (2014). Insights into Mt. Etna's Shallow Plumbing System from the Analysis of Infrasound Signals, August 2007–December 2009. *Pure and Applied Geophysics*, *172*(2), 473–490. <https://doi.org/10.1007/s00024-014-0884-x>
- Taddeucci, J., Alatorre-Ibargüengoitia, M. A., Moroni, M., Tornetta, L., Capponi, A., Scarlato, P., Dingwell, D. B., & De Rita, D. (2012). Physical parameterization of Strombolian eruptions via experimentally- validated modeling of high-speed observations. *Geophysical Research Letters*, *39*(16), 2–7. <https://doi.org/10.1029/2012GL052772>
- Van Daele, M., Moernaut, J., Silversmit, G., Schmidt, S., Fontijn, K., Heirman, K., Vandoorne, W., De Clercq, M., Van Acker, J., Wolff, C., Pino, M., Urrutia, R., Roberts, S. J., Vincze, L., & De Batist, M. (2014). The 600 yr eruptive history of Villarrica Volcano (Chile) revealed by annually laminated lake sediments. *Bulletin of the Geological Society of America*, *126*(3–4), 481–498. <https://doi.org/10.1130/B30798.1>
- Vergnolle, S., & Brandeis, G. (1994). Origin of the sound generated by Strombolian explosions. *Geophysical Research Letters*, *21*(18), 1959–1962. <https://doi.org/10.1029/94GL01286>
- Wang, S. (1996). Finite-difference time-domain approach to underwater acoustic scattering problems, *J. Acoust. Soc. Am.*, *99*(4), 1924–1931, <https://doi.org/10.1121/1.415375>
- Watson, L. M., Dunham, E. M., & Johnson, J. B. (2019). Simulation and inversion of harmonic infrasound from open-vent volcanoes using an efficient quasi-1D crater model. *Journal of Volcanology and Geothermal Research*, *380*, 64–79. <https://doi.org/10.1016/j.jvolgeores.2019.05.007>
- Watson, L. M., Johnson, J. B., Sciotto, M., & Cannata, A. (2020). Changes in Crater Geometry Revealed by Inversion of Harmonic Infrasound Observations: 24 December 2018 Eruption of Mount Etna, Italy. *Geophysical Research Letters*, *47*(19). <https://doi.org/10.1029/20>